RESEARCH ARTICLE

NANO · MICRO small
www.small-journal.com

Chemical-Physical Synergistic Assembly of MXene/CNT Nanocoatings in Silicone Foams for Reliable Piezoresistive Sensing in Harsh Environments

Zuan-Yu Chen, Shuai-Chi Liu, Yu-Xi Wu, Yu-Yue Wu, Li-Dong Peng, Ye-Jun Wang, Feng Nie, Li Zhao, Pei-Yuan Lv, Cheng-Fei Cao, Yang Li, Guo-Dong Zhang, Joonho Bae, Kun Cao, and Long-Cheng Tang**

Owing to their high sensitivity across a wide stress range, mechanical reliability, and rapid response time, flexible polymer foam piezoresistive sensors have been extensively used in various fields. The reliable application of these sensors under harsh environments, however, is severely limited by structural devastation and poor interfacial bonding between polymers and conductive nanoparticles. To address the above issues, robust MXene/CNT nanocoatings on the foam surface, where the chemical assembly of MXene nanosheets and the physical anchoring of CNTs lead to strong interfacial bonding, are designed and described, which endows foams with structural reliability and unexpected multi-functionalities without compromising their instinct properties. The optimized foam nanocomposites thus maintain outstanding wide-temperature flexibility (−60–210 °C) and elasticity (≈3% residual strain after 1000 cycles). Moreover, the nanocomposites display good sensitivity at a relatively wide stress range of 0–70% and remarkable stability under acidic and alkaline settings. Furthermore, the foams with exceptional fire resistance (UL-94 V-0 rating) can provide stable sensing behavior (over 300 cycles) even after being exposed to flames for 5 s, making them one of the most reliable sensing materials so far. Clearly, this work widens applications of flexible piezoresistive sensors based on silicone foam nanocomposites for various harsh environments.

1. Introduction

Flexible polymer-based piezoresistive sensors that can conform to curved surfaces and respond to vast deformation play an vital role in the fields of human-machine interactions, healthcare monitoring, and vapor/gas detection.[1–8] As the demands for practical applications evolve, flexible pressure sensors need to output stable, high sensitivity, and reliable electrical signals for real-time detection.[9,10] By contrast, introducing porous structures into polymer matrices provides new opportunities for flexible sensors since the variation of the conductive path that results from the deformation of skeletons and the mutual contact/separation of pores can lead to higher sensitivity and a wider detection range.[11–13] Therefore, traditional piezoresistive sensors constructed from melamine (MA) and polyurethane (PU) foams have sprung up, which has been recognized as one of the most economical and simple strategies.[14–18] The poor structural strength of these carbonaceous foams, however, tends to degrade and damage under complex conditions e.g. wide-temperature range (−60–210 °C), acidic or alkaline environments, and organic gaseous atmosphere, leading to the loss of electric signals.[19,20] Additionally, some of these foams often trigger catastrophic fire accidents owing to their inherent flammability, which further impedes the applicability of flexible sensors in severe environments.[21]

In comparison with carbonaceous foams, polydimethylsiloxane (PDMS) foams are one of the ideal matrices for fabricating high-performance piezoresistive sensors because the unique Si-O-Si chain endows PDMS polymers with preeminent properties, including mechanical flexibility, hydrophobicity, environmental stability, etc.[22–26] Likewise, due to their inherent electrical insulation, PDMS foams require the construction of conductive paths by incorporating considerable conductive fillers.[12] However, high-content particle filling increases the prepolymer's viscosity, making the foaming process difficult and spelling the agglomeration of nanoparticles, which contradicts the

Z.-Y. Chen, S.-C. Liu, Y.-X. Wu, Y.-Y. Wu, L.-D. Peng, Y.-J. Wang, F. Nie, L. Zhao, P.-Y. Lv, C.-F. Cao, Y. Li, G.-D. Zhang, L.-C. Tang
College of Material, Chemistry and Chemical Engineering
Key Laboratory of Organosilicon Chemistry and Material Technology of MoE
Key Laboratory of Silicone Materials Technology of Zhejiang Province
Hangzhou Normal University
Hangzhou 311121, China
E-mail: lizhao@hznu.edu.cn; lctang@hznu.edu.cn

J. Bae
Department of Nano-Physics
Gachon University
Seongnam-si, Gyeonggi-do 13120, South Korea

K. Cao
State Key Laboratory of Chemical Engineering
College of Chemical and Biological Engineering
Zhejiang University
Hangzhou 310027, China

The ORCID identification number(s) for the author(s) of this article can be found under https://doi.org/10.1002/smll.202406102

DOI: 10.1002/smll.202406102

development of sensors that feature ideal porous structures and sensing properties. Therefore, alternative methods have been dedicated to improving the porous structure and sensitivity of sensors using the blended filler template method,[27,28] template-assisted vapor deposition,[3] 3D printing,[29] and dip-coating method.[30–32] Admittedly, these methods overcome the bad porous structure caused by high-content particle filling and enhance sensitivity of PDMS foams, but strong interfacial bonding between PDMS polymers and nanoparticles has yet to be achieved as a result of the chemical inertia.[33] This poor interfacial bonding definitely result in loss of conductive signals during long-term detection. On the other side, the integration of conductive polymers into PDMS foams, such as poly(3,4-ethylenedioxythiophene): poly (styrene sulfonate) (PEDOT: PSS), has proven to be an effective strategy to address interfacial issues.[34,35] Nonetheless, these conductive polymers can be oxidized or degraded by chemical components found in harsh environments (O_3, H_2O, NO_2, and O_2), which causes decreases in sensitivity and conductivity. As such, it remains a significant challenge to realize remarkable and reliable conductivity in silicone foams. Moreover, to meet the requirements for applications in harsher environments, the flexible polymer foam sensor needs to retain its structural integrity at high temperatures without performance degradation.[36]

Herein, we propose a chemical-physical synergistic strategy to construct firm MXene/CNT nanocoatings on the surface of silicone foams, which provides silicone foams with unexpected multi-functionalities. The MXene nanosheets, which feature metallic conductivity, excellent mechanical performance, and high specific surface area, can be assembled on the surface of silicone foam via silicone chemistry reactions because of plentiful functional groups (e.g. hydroxyl groups) on their surface, thereby forming ultrathin flame-retardant and conductive nanocoatings.[22,37] Furthermore, the expanded molecular space of silicone polymers upon exposure to solvents contributes to the anchoring of 1D nano conductive fillers (e.g. CNTs), further constructing interlaced conductive nanocoatings.[38] The CNT-MXene-assembled silicone foams (MCFs) not only show wide-temperature mechanical flexibility and elasticity at a temperature range of −60–210 °C but also exhibit high sensitivity at a relatively wide stress range of 0–40% and good repeatability and excellent reliability under acidic or alkaline conditions. In addition, the MCF achieves a reliable sensing behavior after being exposed to high-temperature flames for 5 s. This simple strategy can tackle the crucial issue that the poor interface between the PDMS polymers and the conductive nanofillers is poor, affording PDMS foams improved performance metrics and distinctive attributes, which broadens the applications of flexible sensors in harsh environments.

2. Results and Discussion

2.1. Conceptual Design and Material Fabrication

We designed MXene/CNT nanocoatings on the surface of silicone foam using a chemical-physical synergistic strategy to obtain high-performance piezoresistive sensors (**Figure 1**). First, we select a facile room-temperature chemical foaming method to fabricate MXene-assembled silicone foams (MFs).[39] To be specific, hydrogen dimethicone (H-PDMS) cross-links with dihydroxy dimethicone (OH-PDMS) and vinyl dimethicone (Vi-PDMS) via a hydrosilylation reaction to build elastic silicone networks in the presence of Karstedt's catalyst (Figure S1, Supporting Information).[20] At the same time, the single-layered MXene solution directly serves as the foaming agent in the foaming process(Figure S2a,b, Supporting Information). During this process, the hydrophilic hydroxy on MXenes induces MXenes to react with hydrophobic hydrogen dimethicone, which leads to the assembly of MXenes on the foam surface, thus forming an ultrathin MXene nanocoating.[39] This MXene nanocoating predominantly endows silicone foams with excellent fire resistance rather than electrical conductivity since the low content of MXene nanosheets cannot form conductive paths at this stage. Second, to further improve conductivity and facilitate sensitivity, we utilize an ultrasound-assisted anchoring method to assemble 1D CNTs (Figure S2c, Supporting Information) on the foam surface. When exposed to isopropanol, the incompletely cured PDMS polymer networks tend to swell and expand, which provides sufficient gaps for anchoring CNTs. With ultrasonic assistance, CNTs are easily anchored on the foam surface.[26,38,40] As the MCFs are heated and the isopropanol evaporates, the expended molecular networks further crosslink and contract, fasten the CNTs, and eventually form interlaced MXene/CNT nanocoatings. This dual strategy ensures the reliable assembly of interlaced conductive and fireproof nanocoatings without compromising silicone foams' intrinsic properties, therefore enhancing the all-around properties of the silicone foam nanocomposites.

2.2. Material Characterization, Structure Analysis, and Performance Optimization

On the basis of the conceptual design, we next characterize the morphology and structure of MCFs and optimize the relationship between conductivity and process parameters. The SEM images reveal that the sizes of porous configurations of SiFs, MFs, and MCFs are similar, with diameters ranging from 100–300 µm, indicating that our unique fabrication process does not negatively impact porous structure (**Figure 2**a,d; Figure S3, Supporting Information). The MXene nanosheets are well bonded to the foam surface, showing a good interface (Figure 2b).[20] The EDS mapping displays that C, O, Ti, and Si are uniformly distributed, without concentration of any element. This phenomenon means that MXene nanosheets are coated with a thin layer of silicone rubber, which can effectively prevent MXenes from oxidation under harsh environments (Figure 2c). The CNTs that closely anchor on the foam surface create an interlaced conductive and fireproof nanocoating with MXene nanosheets (Figure 2e). The cross-section SEM images show that the CNTs are embedded in the surface of foams, and in turn, the internal skeletal structure remains smooth, which can preserve the intrinsic properties of silicone foams to the greatest extent (Figure 2f). Moreover, the characteristic peaks of —OH (MXene nanosheets), Si—OH (OH-PDMS), and Si-Vi (Vi-PDMS) are absent from MFs, as evidenced by FT-IR spectra, indicating the formation of the crosslinking networks and covalent bonds between MXenes and silicone polymers via organosilicon chemical reactions (Figure 2g; Figure S4, Supporting Information). On the other hand, the MFs present a

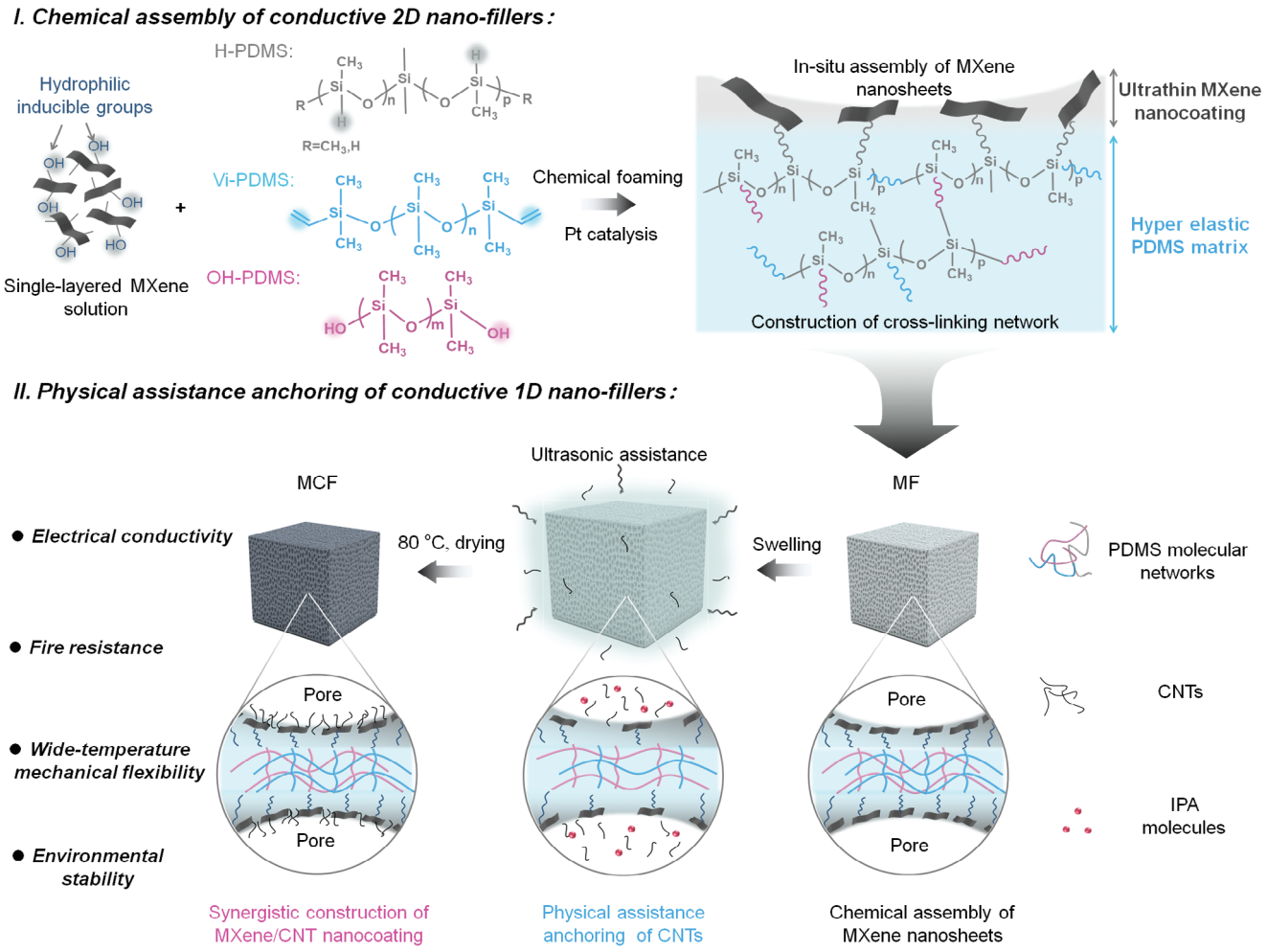

Figure 1. Conceptual design and material fabrication

weak peak of Si—H in contrast to MCFs, which means that polymeric networks are not fully constructed. Thus, the surface of MFs can accommodate more CNTs during the anchoring. Aside from the solo peak of Si—O—Si of the SiF, the existence of the weak peaks of C—Ti—O—Si and C—Ti—O further confirms the covalent bonds between MXenes and silicone polymers in MFs (Figure 2h).[37] The conductivity is positively related to ultrasonic-assisted coating time (The CNTs dispersion was changed every 2 h to prevent CNTs from breakage). The threshold value of conductivity of MCFs is ≈0.145 S cm^{-1} corresponding to ultrasonic-assisted coating time of 8 h and the CNTs content of ≈12 wt.%, indicating that further increasing coating times only slightly enhance the conductivity of MCFs (Figure 2i). In comparison with CNTs-assembled silicone foams (CFs, which are prepared from pure silicone foams embedded with CNTs), the MXene nanocoating mildly improves the conductivity of MCFs, which demonstrates synergistic conductivity between MXenes and CNTs. Anchoring CNTs on the foam surface improves surface roughness, and the MCFs achieve a water contact angle of ≈143° compared to 130° for MFs, which enhances the environmental stability (Figure 2j; Figure S5, Supporting Information). The MCFs show a relatively low density of ≈200 mg cm^{-3}, achieving a trade-off between high conductivity and high porosity (Figure 2k). All tests are done on foam materials that have an ultrasonic-assisted time of 8 h unless otherwise noted.

2.3. Mechanical Flexibility in a Wide Temperature Range

We investigated the compressive properties of the MCFs with uniaxial quasi-static compression at a strain range of 25 – 75%. The sample is compressed from 10 to 2.5 mm and entirely recovers the initial state after the removal of force. The stress-strain curves exhibit closed hysteresis loops without dramatic changes, which are characteristic of viscoelastic, energy-dissipative, and highly deformable materials (**Figure 3a**).[41–43] The maximum stress at 75% strain is 60.2 kPa, indicating that the MCFs can support up to ≈3000 times their own weight without structural collapse. The MCFs can be repeatedly compressed at 50% strain for 1000 times at 30 °C. The 1000th hysteresis loop is similar to 1st cycle, with unnoticeable stress degradation and plastic deformation, less than 4% and 0.1%, respectively, showing outstanding elasticity (Figure 3b). In addition, the almost constant maximum stress (≈8 kPa), energy loss coefficient (≈0.1), and Young's

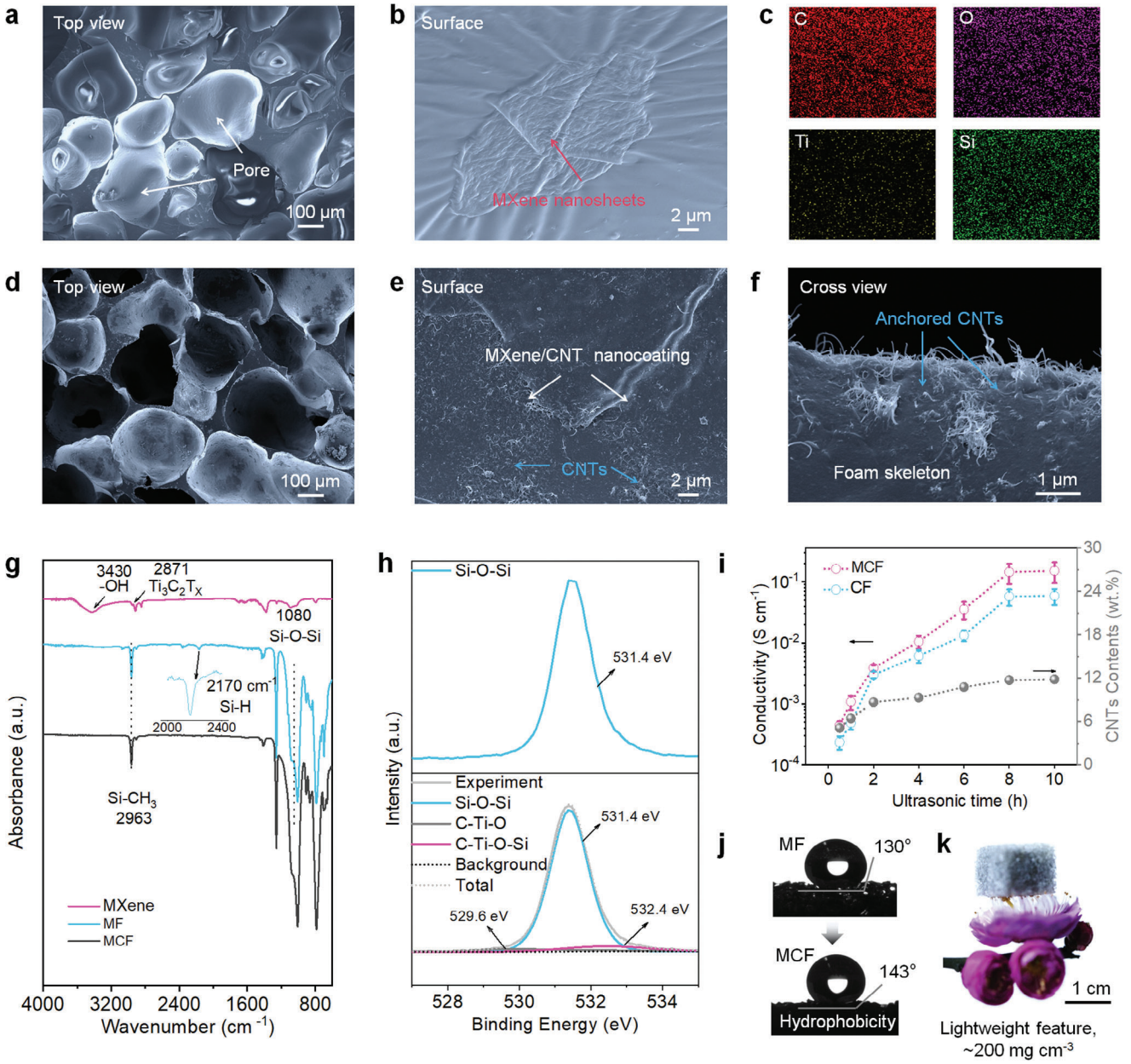

Figure 2. Material characterization, structure analysis, and performance optimization. a,b) SEM images of MFs. c) Corresponding elemental analysis in Figure 2b. d–f) SEM images of MCFs. g) FT-IR spectra of Mxene nanosheets, MFs, and MCFs. h) XPS-O1s peak spectra of SiFs and MFs. i) Variations in sensor resistivity and CNTs contents as a function of ultrasonic time. j) Variations in contact angle of water before and after coating with CNTs for 8 h. k) Optical images showing a Chinese Plum with an MCF on its top, demonstrating a lightweight property of MCFs.

modulus (≈5 kPa) further demonstrates the elasticity of MCFs. Typical stress-strain curves of MCFs at compression 50% at −60, 30, 120, and 210 °C maintain closed hysteresis loops, indicating excellent wide-temperature mechanical compressive properties (Figure 3d). Moreover, cyclic compressive tests at −30 and 210 °C also reveal that the compressive curves retain virtually consistent after 100 compression cycles, with only slight strength degradation of 0.5% and 0.7%, respectively, which demonstrates wide-temperature mechanical flexibility and reliability (Figure 3e).

Apart from outstanding compressive performance, the MCFs also present remarkable flexural flexibility with a bending strain up to 60%, without fracture failure and visible stress degradation observed (Figure 3f). The 100th cycle loop remains nearly unchanged compared with the 1st cycle, indicating their superb flexibility against continual bending (Figure 3g). We next tested the stretchability of the CSFs with uniaxial quasi-static tension. The sample is stretched from 15% to 45% and completely recovers after stretch stress release, showing good stretchability (Figure 3h). The tensile fracture strain reaches up to 115%, which has a fracture stress of 22 kPa (Figure S6, Supporting Information). The flexibility of the MCFs benefits from unique silicone polymer chains that have a lower potential barrier of rotation

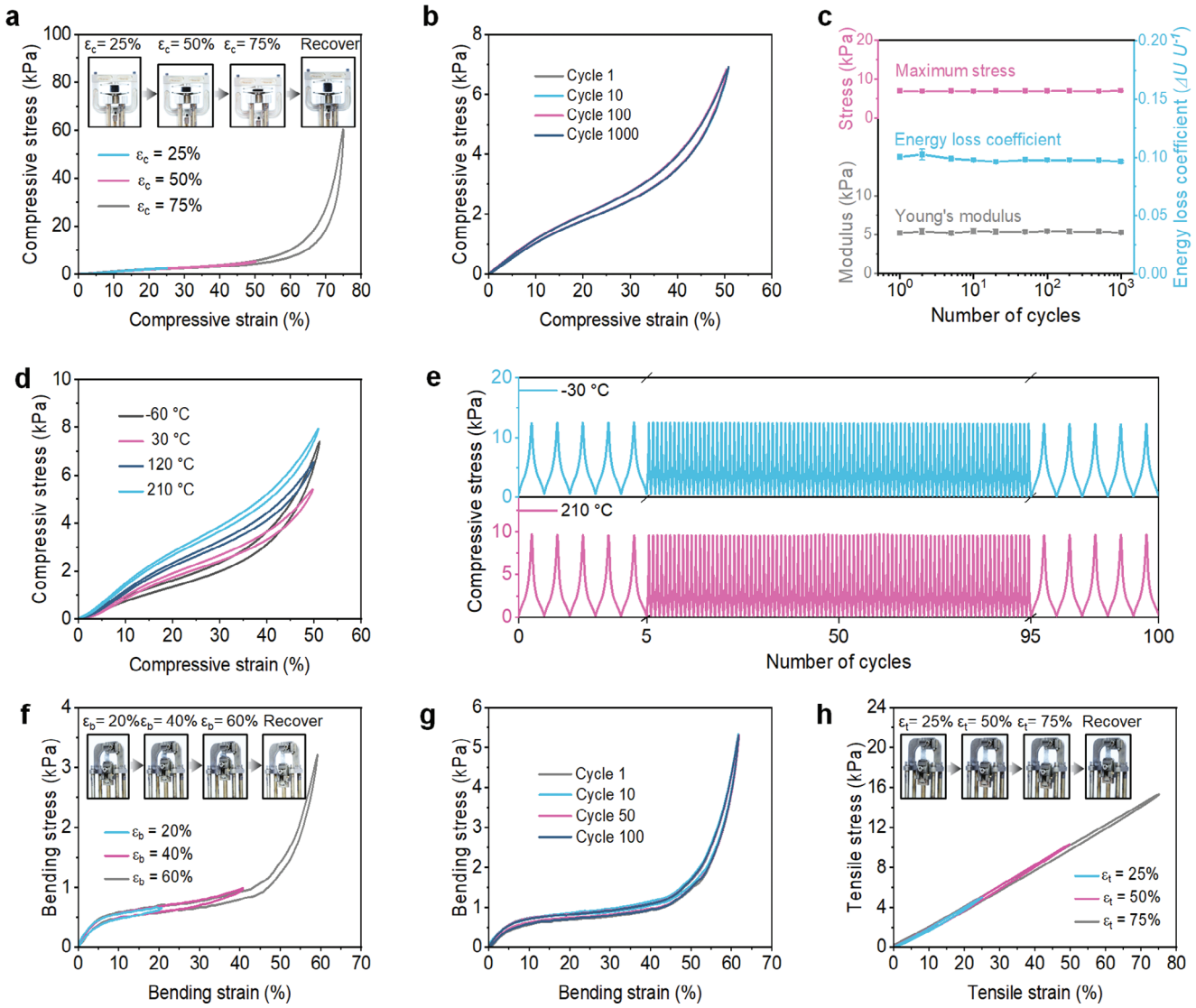

Figure 3. Mechanical properties. a) Uniaxial compression of MCFs with strain up to 70%. Inset: Snapshots of one cycle. b) Compressive stress-strain curves of MCFs at 50% strain for 1000 cycles. c) Cyclic dependencies of Young's modulus, loss modulus, and damping ratio. d) Compressive stress-strain curves of CMFs at 50% strain at −60, 30, 120, and 210 °C. e) Compressive tests of MCFs at 50% strain for 100 cycles at −30 and 210°C. f) Bending test of MCFs with strain up to 60%. Inset: Snapshots of one cycle. g) Bending stress-strain curves of MCFs at 60% strain for 100 cycles. h) Tensile test of MCFs with strain up to 45%. Inset: Snapshots of one cycle.

(<0.8 kJ mol^{-1}) and a large bond angle (143°), which makes the MCFs flexible.[25,44] All mechanical tests demonstrate that our unique assembly strategy retains the mechanical flexibility of MCFs, thus laying a foundation for the development of high-performance pressure sensors in practical applications.

2.4. Pressure Sensing Performance and Low Concentration Volatile Organic Compounds Detection Performance of the MCFs

We next evaluated the piezoresistive performance and organic volatile compounds detection capabilities of the MCFs. The MCFs exhibit resistance response behaviors with increases in the applied pressure, characterized by three major regions (**Figure 4a**). Specifically, the MCFs show a slow increase in $\Delta R/R_0$ with a gauge factor (GF) of 1.49 within a strain range of 0 – 20%. As the applied strain increases from 20% to 45%, the foams exhibit a gradually steeper increase in $\Delta R/R_0$, achieving a GF of 2.42. Further increases in applied strain result in a slow increase in $\Delta R/R_0$ with a GF of 0.45, extending up to a strain range of 70%. These results indicate that MCFs have a relatively wide stress range of 0 – 70% and good sensitivity. Notably, the MCFs can immediately output resistance response signals while loading a 0.6 g glass bead, showing an extremely low detection limit (Figure 4b). The current-voltage (*I–V*) curves of the sensor precisely conform to Ohm's law, with the slope increasing as pressure increases due to corresponding decreases in resistance at different pressure levels. This behavior demonstrates excellent

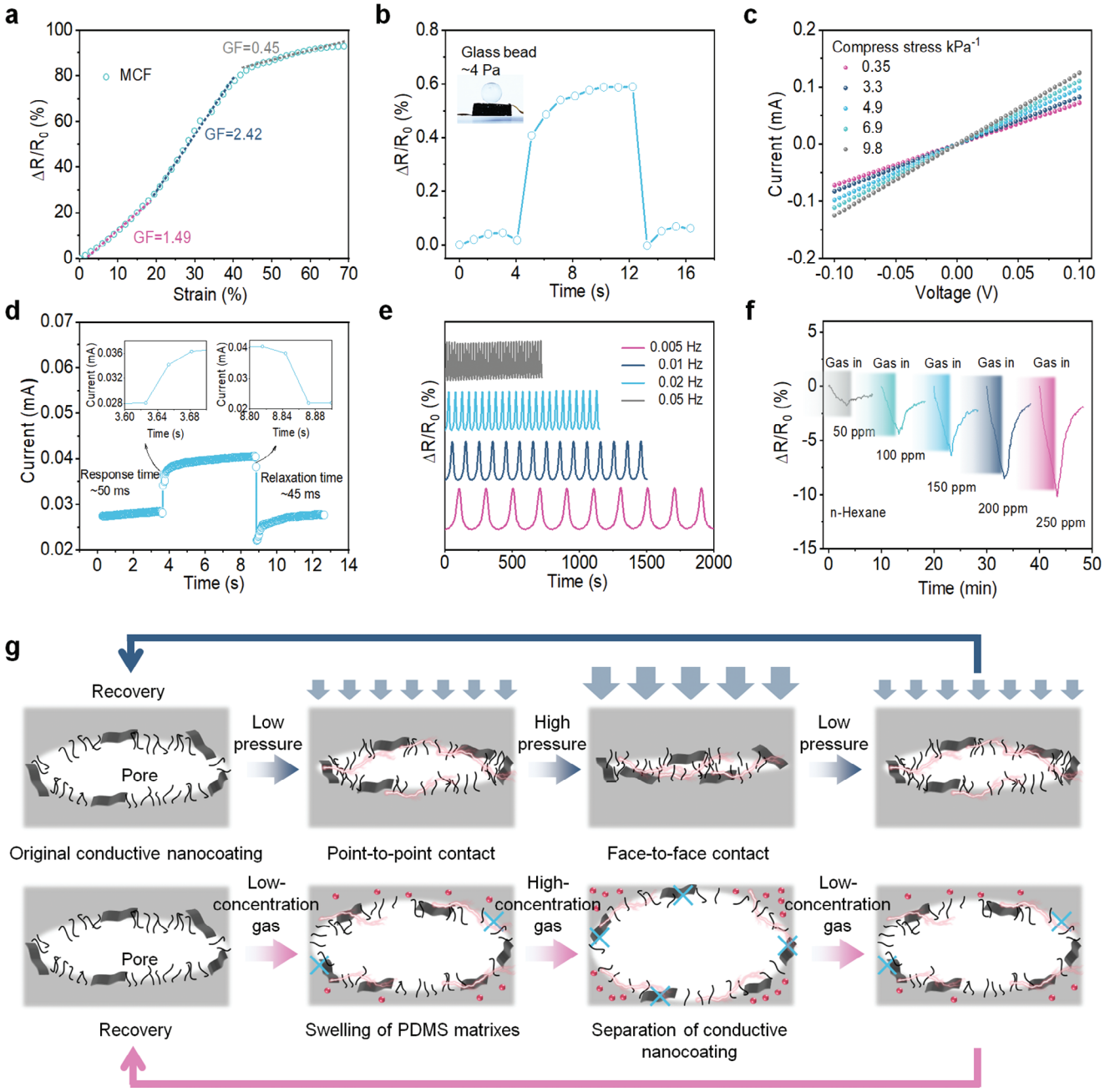

Figure 4. Sensing properties and the mechanism of MCFs. a) Relative resistance variations of MCFs, $\Delta R = R_0\text{-}R$, R_0 is initial resistance and R is the resistance with external pressure; gauge factor (GF) generally defined as the slope of the relative resistance variation $((\Delta R/R_0)/\ \Delta P$ where *P* is the pressure difference) is calculated to reflect the sensitivity to applied strain. b) Relative resistance variations of MCFs while loading a glass bead. The inset shows the corresponding optical image of the object. c) Current-voltage (*I–V*) curves of MCFs under different pressure conditions. d) Relative resistance variations of MCFs during the loading and the unloading process; the insets show magnified images of response edges during the loading and the unloading. e) Frequency dependence of resistance variations. f) Relative resistance variations toward different concentrations of organic volatile compounds. g) Schematic diagram of the sensing mechanism under pressure conditions and organic gas environments.

reliability in the compression process (Figure 4c). Additionally, the MCFs also exhibit a fast response time of ≈50 ms and a recovery time of ≈45 ms, comparable with the response of human skin (30–50 ms), indicative of an outstanding response behavior (Figure 4d).[45,46] To evaluate the repetition of the sensor, we investigated the $\Delta R/R_0$ responses as a function of time during compression-recovery cycles. The $\Delta R/R_0$ response to a pressure of 1 kPa demonstrates reliable durability across frequencies ranging from 0.005 to 0.05 Hz, and the peak variations of the response signals are almost consistent in the different frequencies (Figure 4e). More importantly, the MCFs demonstrate high sensitivity and a vast sensing response range (50–250 ppm) for

detecting organic volatile compounds, making them highly suitable for real-time and continuous monitoring of organic gases to ensure environmental safety (Figure 4f).

The above outstanding sensitive properties of the MCFs are related to their structural evolution caused by external factors. As shown in Figure 4g, the interlaced MXene/CNT nanocoatings on the foam surface provide the initial electrical conductivity for porous composites. Under slight pressure or exposure to low-concentration organic volatile compounds, partially exposed CNTs begin to contact or separate, which yields a mild resistance variation. As the porous structure offers sufficient space for deformations, further increasing external pressure or organic volatile compounds exposure time can generate face-to-face contacts or separations of conductive nanocoating, which results in an abrupt resistance change. Therefore, these processes effectively generate or eliminate conductive paths, thereby leading to significant signal variations in MCFs.[38]

2.5. Applications of MCFs for Various Detection Under Harsh Conditions

The ability to adapt to curved surfaces and resist harsh environments allows MCFs to be used in various practical applications. We attach MCFs to various positions on volunteers using transparent tape to detect a range of physiological signs and practical body motions. Whether the volunteer performs a faint cheek blow or a vigorous finger bend, the MCF can accurately output distinct changes in electrical resistance, with a range from 0 – 10% and 0 – 75%, respectively, which demonstrates that our sensors show great promise in healthcare monitoring (**Figure 5**a). Aside from the pressure sensing, the sensor exhibits significant variations in resistance from 0 – 58% when it encounters a variety of organic volatile compounds, such as n-hexane, ethyl acetate, cyclohexane, and so on. The variations are positively related to the polarity of solvents while negatively to the size of solvent molecules. It also exhibits excellent repeatability (the first responsivity of the sensor is similar to the subsequent two cycles), showing potential for early detection of organic gas leaks (Figure 5b).

The MCFs repel various liquids, including water, acid, alkali, and saline, with contact angles of 142–144°, and exhibit an obvious silver mirror phenomenon underwater (Figure 5c; Figure S7, Supporting Information). Because of the rough morphology created by the nanocoating and the low surface energy of silicone polymers, the surface of the MCF can endow water droplets with Cassie state, thus providing long-term environmental stability (Figure 5d).[1,47–49] Hence, even after 30 days of saturation in various liquids, 200 cycles of compression, or exposure to extreme temperature environments (−25 to 125 °C) and different media (air, water, and saline solution), the contact angle of water and resistance are almost invariable, making MFCs feasible to detect in harsh environments (Figure 5e,f; Figures S8 and S9, Supporting Information). Based on that, we detect electric signals of finger bending behaviors in water with different temperatures (Figure 5g). As expected, the signals that change from 0 to 75% are still stable and repetitive, which turns out the reliability of MCFs in aquatic environments (Figure 5h). Moreover, reliable resistance responses of MCFs in extreme temperature environments and different media are nearly consistent without significant fluctuation, further exhibiting their environmental stability (Figure 5i; Figure S10, Supporting Information). As a consequence, the MCFs exhibit reliable sensing behaviors under complex conditions, which present promising applications in harsh settings.

2.6. Fire Resistance, Thermal Stability, and Sensing Reliability after Exposure to Flames

We next evaluated the thermal stability and fire resistance of various foams through vertical burning tests and limiting oxygen index (LOI) texts because these properties are crucial for their application in harsh environments. When exposed to methane flames, the SiFs burn violently and have a limited LOI value of 21.6%, showing poor flame retardancy (**Figure 6**a,b). Compared with the SiFs, the CFs only exhibit a slight improvement in fire resistance, with an LOI value of 22.6% and no UL-94 rating (Figure S11a, Supporting Information). Interestingly, the assembly of MXenes substantially improves the flame retardancy of the SiFs. As shown in Figure S11b (Supporting Information), the MFs, with an LOI value of 27.0%, pass a UL94 V-0 rating. These results indicate that the assembly of MXenes on the surface of silicone foams predominately contributes to fire resistance, whereas that of CNTs to conductivity. The MCFs display the highest LOI (27.2%) and can self-extinguish in 4 s after each flame attack, achieving a UL-94 V-0 rating (Figure 6c; Figure S12, Supporting Information). These results mean that MXenes and CNTs synergistically improve the flame retardancy of silicone foams. We further investigated the thermal stability of different foams using thermogravimetric-Fourier transform infrared spectroscopy (TG-IR). The MCFs exhibit an excellent thermal decomposition temperature ($T_{5\%}$ = 383 °C) and char yield (65.4%) in the air atmosphere, which are higher than that of SiFs ($T_{5\%}$ = 381 °C and 23.9%, respectively) (Figure 6d). The absorbance of volatile species of the SiFs in 3D IR spectra is much more intense than that of MCFs, indicating that MXenes and CNTs suppress the decomposition of silicone polymers (Figure 6e,f).[50] The superb fireproof property and thermal stability mainly benefit from the formation of the compact nano-silica/TiO_2 protective layer during the combustion that prevents the internal PDMS molecules from thermal degradation.[22,37,39,51,52] On the contrary, PU foams show poor thermal stability and degrade only at 264 °C, which limits their applications in harsh conditions (Figure S13, Supporting Information).[19,21]

Combined with electrical conductivity and fire resistance, MCFs offer new opportunities for sensing applications under the harsher environments. Key opportunities include situations where critical real-time signals need to be monitored, where objects are likely to be exposed to high-temperature flames, and where a high risk of fire requires restriction. To illustrate the reliability of the MCFs in more severe environments, we show that the MCFs can still output cyclic and stable electrical signals even after being exposed to high-temperature flame (>500 °C) for 5 s. Upon exposure to the flame, the CF can be ignited immediately and burns fiercely after the removal of the flame. Thermal imaging indicates that the temperature of CFs is as high as 741 °C (Figure 6g,h). As it turned out, the CF is fully

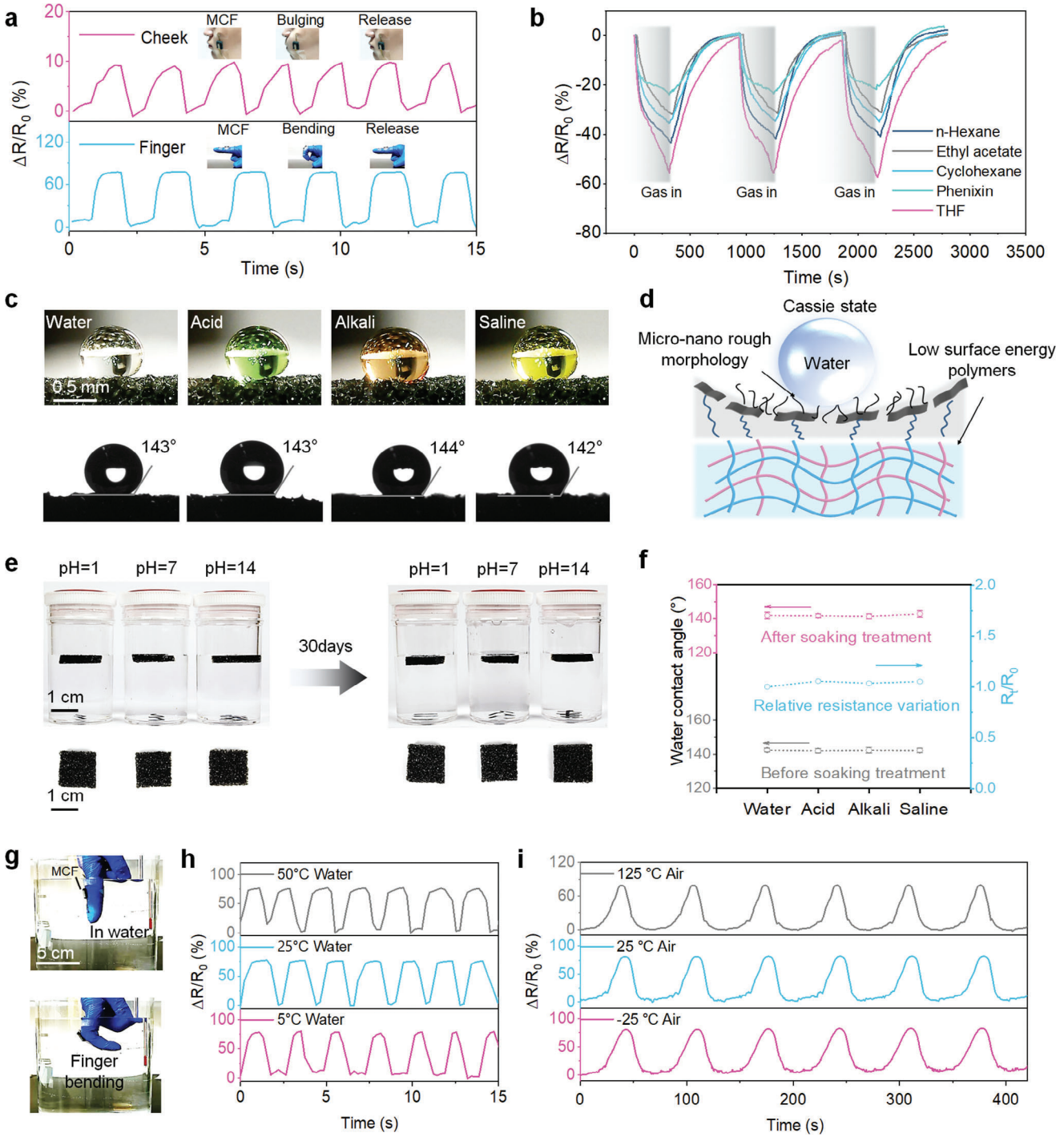

Figure 5. Applications of MCFs for various detection under harsh conditions. a) Relative resistance variations of sensors with facial motions and finger motions. b) Relative resistance variations toward various organic volatile compounds. c) Hydrophobicity of MCFs toward various liquids. d) Schematic illustration of the Cassie state for MCFs. e) Of MCFs immersed in various liquids for 30 days, optical images show good structural stability. f) Variations of the contact angle of water and relative resistance before and after immersing in different liquids for 30 days. g) Finger-bending behaviors in water. h) Variations of the relative resistance of MCFs toward a finger with bending-release motions immersed in water at different temperatures. i) Variations of the relative resistance of MCFs in air at different temperatures.

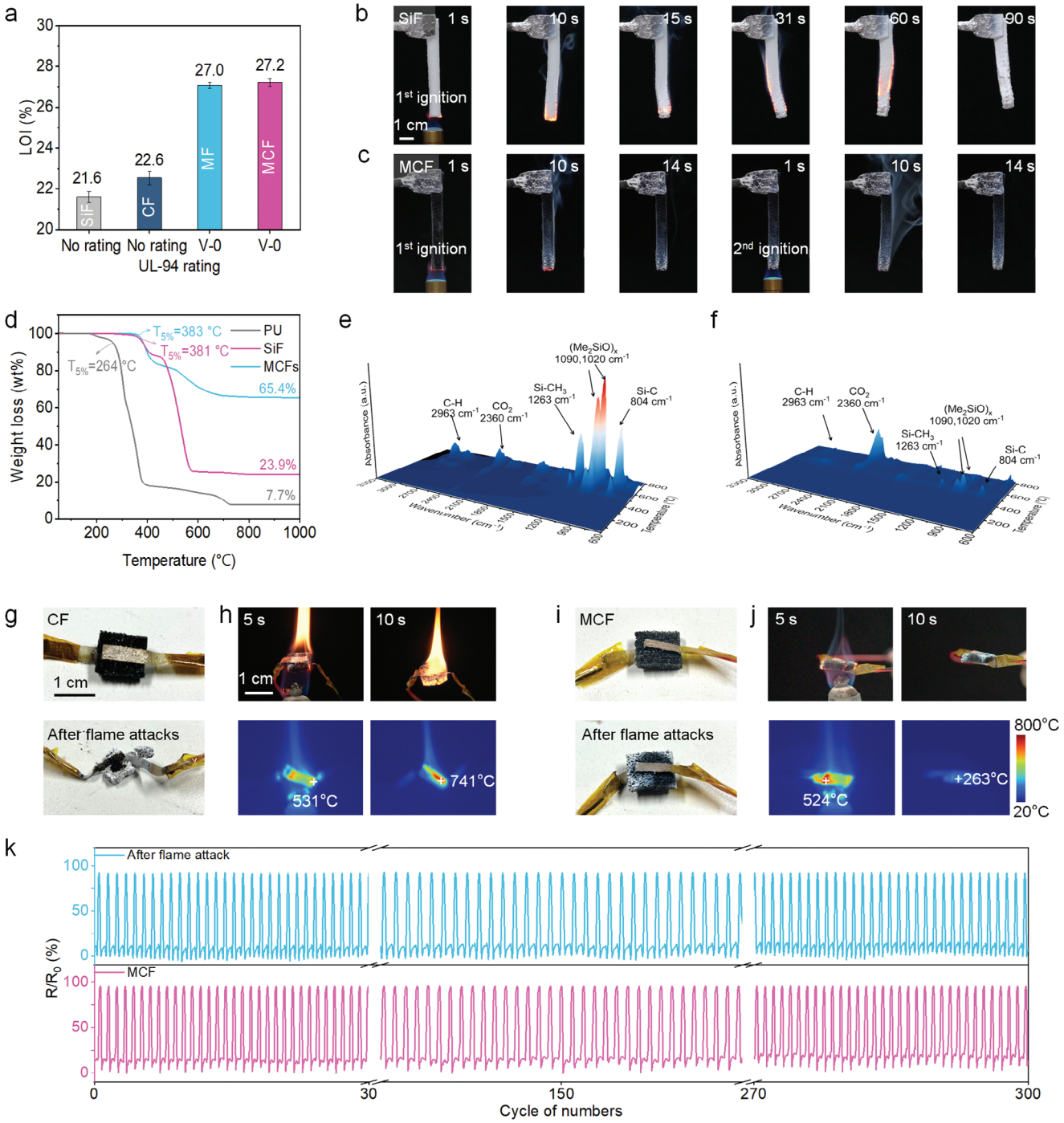

Figure 6. Fire resistance, thermal stability, and sensing reliability after exposure to flames. a) LOI values and UL-94 rating for various foams. Vertical burning tests for (b) SiFs and (c) MCFs. (d) TGA results for PU foams, SiFs, and MCFs. 3D IR results of (e) SiFs and (f) MCFs. (g) Optical images of CFs before and after being exposed to flame for 5 s. h) The burning process of CFs and corresponding infrared images. i) Optical images of MCFs before and after being exposed to flame for 5 s. j) The burning process of MCFs and corresponding infrared images. k) The variation of the relative resistance of MCFs before and after the flame attack.

damaged and leaves behind a loose structure without any sensing property. By contrast, the MCF with a thickness of 3 mm exhibits superb fire resistance and can self-extinguish within 5 s after exposure to flame for 5 s even though the temperature is up to 524 °C (Figure 6i,j). More importantly, the MCF maintains reliable sensing properties, which can constantly output electrical signals (Figure 6k). The MCFs therefore show great prospects for reliable detection associated with harsh environments under which conventional sensors could easily collapse, ignite, or show poor electrical conductivity and significantly encourage the

Table 1. Comparison of processing, filler type and content, density, electrical conductivity, LOI value, and UL-94 rating of as-designed MCF with previous silicone foam-based nanocomposites.

Processing condition	Filler type	Filler content [wt.%]	Density [g cm^{-3}] (Composites/matrix)	Electrical conductivity [S cm^{-1}]	LOI value [%] and UL-94 rating	Refs.
Ni-foam based template	[a] CNF	1	0.05-0.20	10^{-17}	–	[11]
		12		10^{-8}		
		28		6.7×10^{-7}		
Ni-foam based template	[b] CNTs/GO	0.1	0.10	10^{-7}	–	[30]
		1.5		0.112		
		2.5		0.135		
Sugar particle-based template	CNF	0.1	0.23	0.0001	–	[32]
		0.7		0.0065		
		2.8		0.042		
Salt particle-based template	[c] CB in ethyl alcohol	0.1 g/80 ml	0.13	8.3×10^{-6}	–	[54]
		0.3 g/80 ml		2.5×10^{-5}		
		0.5 g/80 ml		6.7×10^{-5}		
		1.0 g/80 ml		2×10^{-4}		
Salt particle-based template	CNTs	1	–	1.4×10^{-12}	–	[2]
		10		1.0×10^{-6}		
		30		4.05×10^{-5}		
Supercritical CO_2 foaming	CNTs	2	–	10^{-7}	–	[55]
		10		0.0001		
		15		0.0011		
Supercritical CO_2 foaming	[d] MWCNTs + Fe_3O_4	5 + 10	0.32 (10 wt.% MWCNTs)	3×10^{-5}	–	[56]
		10 + 10		0.15		
		10 + 20		0.2		
Phase separation techniques	[e] CNTs-GR (5:1)	0.3	–	2×10^{-6}	–	[27]
		0.9		8×10^{-4}		
		1.3		7×10^{-3}		
3D printing of polymer particle-based template	Graphene nanoplatelets	5-coating times	0.3–0.7	3×10^{-8}	–	[29]
		10-coating times		1×10^{-6}		
		15-coating times		2×10^{-5}		
		20-coating times		1×10^{-4}		
Chemical foaming techniques	[f] A-MWNT and GO (4:1)	5	0.46	10^{-16}	–	[57]
		10	0.38	2×10^{-10}		
		15	0.68	1.26×10^{-8}		
		20	0.72	1.17×10^{-8}		
Chemical foaming and self-adhesive design	MXene/cellulose	8	0.24/0.22	0.067	27.6/V-0	[22]
Chemical foaming techniques	MXene/CNT	8.7	0.2	0.0039	27.2/V-0	This work
		12		0.145		

[a] CNF: carbon nanofiber; [b] CNTs/GO: carbon nanotubes and graphite oxide; [c] CB: carbon black; [d] MWCNTs: multiwalled carbon nanotubes; [e] CNTs-GR: carbon nanotubes and graphene; [f] A-MWNT: acid multi-walled carbon nanotubes.

all-round development of piezoresistive sensors with high performance and distinguished attributes (**Table 1**).

3. Conclusion

In summary, we report a chemical-physical synergistic strategy to assemble MXene/CNT nanocoatings in silicone foams that overcome the problem of poor interfacial bonding between silicone polymers and conductive nanoparticles. Benefiting from the hybrid nanocoatings, MCFs thus acquire unexpected structural reliability and multi-functionalities – wide-temperature flexibility, electrical conductivity, fire resistance, and surface hydrophobicity for example – which makes it prospective for piezoresistive sensors to reliably detect in complex settings, such as acidic, basic, and saline conditions. Moreover, the MCFs can still output stable electrical singles even after being exposed to high-temperature flames. As a result, this unique strategy expands the application of silicone foams in diverse areas, including aviation, biomimetic robotics, oil environments, deep-sea exploration, and beyond.

4. Experimental Section

Materials: Vinyl terminated dimethicone (Vi-PDMS, viscosity: 50000 cP), Hydroxyl terminated dimethicone (OH-PDMS, viscosity: 5000 cP), and hydrogen dimethicone (H-PDMS, hydrogen content: 1.6%) are purchased from Xinan Chemical Corporation, China. Ti_3AlC_2 precursor (MAX) was purchased from Jilin Technology Co., Ltd. Karstedt platinum catalyst is obtained from Betely-Polymer Materials Co., Ltd.

Carbon nanotubes (CNTs) were bought from Showa Denko Co., Ltd., Japan. Isopropanol (IPA), phenixin, ethyl acetate, cyclohexane, h- hexane, lithium fluoride salt (LiF) with a purity of 98%, and hydrochloric acid (HCl) with a concentration of 35%were obtained by Sinopharm Chemical Reagent Co., Ltd. (China). The inhibitor (1,3,5,7-Tetravinyl-1,3,5,7-tetramethylcyclotetrasiloxane) was obtained from Zhejiang Runhe Chemical New Material Co., Ltd. (China). All chemicals were used without purification.

Materials Characterization: SEM micrographs were obtained with a field emission scanning electron microscope (ZEISS Sigma-500) at a voltage of 3 kV in SE2 mode. The elements of MFs were analyzed by an SEM-EDX instrument (ZEISS Sigma-500). Fourier transform infrared spectrometer was used by the wavelength scanning test at the range of 4000–600 cm^{-1}, and the instrument model was Bruker Alpha-T. The thermogravimetric analysis/infrared spectrometry (TG-IR) was performed using the TGA Q500 thermogravimetric analyzer which was coupled with the Nicolet 6700 FT-IR spectrophotometer via the transfer line, and the heating rate is 10 °C min^{-1}. Compressive, bending, tensile, and viscoelastic tests were carried out using a DMA instrument (TA-Q800). Two pieces of copper foil were carefully fixed on the opposite surface of the foam by silver paste, and then connected to the analyzers by copper wires. The initial resistance and the real-time resistance variations during the sensing behaviors testing were measured by a source meter (2601B, Keithley, America). For the compressive tests, the sample size was 10 × 10 × 10 mm^3, and the compression rate was 0.3 mm min^{-1}. The sample size for the bending tests and tensile tests was 30 × 5 × 2 mm^3, and the bending and tensile rate was 0.5 mm min^{-1}. The surface hydrophobic properties of various samples were obtained with a DSA30 CA analyzer (Kruss, Germany) using a 3 µL water droplet, and the reported results are the average value of five parallel measurements. The limited oxygen index (LOI) of various foams was analyzed via a JF-3 oxygen index instrument (Jiangning, China) with a sample size of 100 × 10 × 10 mm^3, according to ISO4589-2:1996. The UL-94 vertical burning test was obtained by a 5402H-V BURNING TESTER instrument and the sample size was 130 × 13 × 10 mm^3, test standard according to ASTM D 3801. The infrared images of samples were measured by Fluke Ti450pro (−20–1500 °C), and the emissivity is 0.98. The Volatile Organic Compounds (VOCs) sensing testing was measured by a homemade measurement device, including mass flow controllers (MFCs), solvent bubbles, a gas detection chamber (500 mL), and a source meter. First, the resistance of the sample under dry air was recorded for 50 s to get the baseline; after that, the sensing behavior was measured by exposing the sample to organic vapor for 100 s and then drying it in air for 200 s at 25 °C. Two MFCs were employed to control the gas flow rates and the concentration of target vapors, the total flow rate was kept at 500 cm^3 min^{-1}. The concentration of the VOCs (c) was calculated by Equation (1)

$$c\ (\%) = \frac{100 P_i f_i}{p\,(f_1 + f_2)} \quad (1)$$

where P is the atmospheric pressure (101.3 kPa), and Pi is the saturated vapor pressure of target solvent at 25 °C, f_1 and f_2 are the flow rate values of organic vapor (controlled by the MFC1) and dry air (controlled by the MFC2), respectively.[11]

Preparation of MXene Aqueous Solution: Ti_3C_2Tx MXene sheets were synthesized by the procedure described in previous works. Initially, MAX was added to a solution consisting of 30 mL volume and 9 mL of HCl, containing 3 g of LiF. The mixture was stirred at 35 °C for 48 h. After the reaction, the suspension was subjected to sonication for 0.5 h to obtain the dispersed Ti_3C_2Tx nanosheets. Subsequently, the dispersion was washed and centrifuged repeatedly until the pH reached ≈6. Finally, a dark green MXene/water dispersion with a certain concentration was obtained, and the resulting sediment was dispersed in 100 mL of deionized water.[22,53]

Fabrication Process of CNT Dispersion: 0.25 g CNTs and 100 mL isopropanol are mechanically mixed at a speed of 500 rpm for 30 min to obtain a mixture. Then the mixture was dispersed by sonication for 30 min, and the homogeneous CNTs dispersion was obtained.

Fabrication Process of SiFs: First, 40 g Vi-PDMS, 50 g OH-PDMS, 10 g H-PDMS, inhibitor, and 4 g water are mechanically mixed at a speed of 1200 rpm for 5 min to obtain a homogeneous mixture. Second, 0.8 g Karstedt catalyst (3000 ppm) is added to the above mixture and stirred for 60 s. Then, the mixture is transferred to the mold, foaming at room temperature for 15 min, and the SiF is obtained. Finally, the SiF is cured in an oven at 80°C for 2 h.

Fabrication Process of MFs: First, 40 g Vi-PDMS, 50 g OH-PDMS, 10 g H-PDMS, inhibitor, and 5 g MXene dispersion (100 mg g^{-1}) are mechanically mixed at a speed of 1200 rpm for 5 min to obtain a homogeneous mixture. Second, 0.8 g Karstedt catalyst (3000 ppm) is added to the above mixture and stirred for 60 s. Then, the mixture is transferred to the mold, foaming at room temperature for 15 min, and the MFs are obtained.

Fabrication Process of CFs: First, the SiFs were dipped into the CNTs dispersion in a beaker. After the foam was filled with CNT dispersion, the entire beaker was ultrasonically treated for 2–10 h at the power of 300 W to anchor CNTs on the foam surface. Finally, the sample fully dried out in an 80 °C oven for 2 h.

Fabrication Process of MCFs: The fabrication process of MCFs was the same as the CFs.

Supporting Information

Supporting Information is available from the Wiley Online Library or from the author.

Acknowledgements

This work was financially supported by the National Natural Science Foundation of China (52373033, 12002113, and 51973047), the Key R&D Program Project in Zhejiang Province (2024C01194), and the Science and Technology Key Project of Zhejiang Province (LZ22E030002). Thanks to Shiyanjia Lab (www.shiyanjia.com) for the testing services. The institutional ethics committee confirmed that no ethical approval is required for these experiments. The authors would like to thank Shuai-Chi Liu for his participation in the physiological signal measurements, who took part with informed consent.

Conflict of Interest

The authors declare no conflict of interest.

Author Contributions

Z.-Y.C., S.-C.L., and Y.-X.W. contributed equally to this work. Z.-Y. C. performed conceptualization, methodology, investigation, validation, experiment, data curation, formal analysis, and wrote original draft preparation; S.-C.L. performed methodology, investigation, data curation, and formal analysis; Y.-X.W. performed methodology, investigation, validation, experiment, data curation, and formal analysis; Y.-Y.W. performed methodology and investigation; L.-D.P., Y.-J.W., F.N., P.-Y.L., Y.L., G.-D.Z., K.C., and J.B. performed investigation; L.Z. performed conceptualization, supervision, funding acquisition, and wrote, reviewed & edited; C.-F.C. performed methodology and investigation; L.-C.T. performed conceptualization, supervision, funding acquisition, and wrote, reviewed & edited.

Data Availability Statement

The data that support the findings of this study are available in the supplementary material of this article.

Keywords

chemical-physical synergistic assembly, harsh environments, multifunctionalities, MXene/CNT nanocoatings, polymer foam piezoresistive sensors

Received: July 20, 2024
Revised: September 24, 2024
Published online: October 30, 2024

[1] W. Cheng, X. Wang, Z. Xiong, J. Liu, Z. Liu, Y. Jin, H. Yao, T. S. Wong, J. S. Ho, B. C. K. Tee, *Nat. Mater.* **2023**, *22*, 1352.
[2] Y. J. Fan, X. S. Meng, H. Y. Li, S. Y. Kuang, L. Zhang, Y. Wu, Z. L. Wang, G. Zhu, *Adv. Mater.* **2017**, *29*, 1603115.
[3] N. P. Luo, Y. H. Huang, J. Liu, S. C. Chen, C. P. Wong, N. Zhao, *Adv. Mater.* **2017**, *29*, 1702675.
[4] S. Jung, J. H. Kim, J. Kim, S. Choi, J. Lee, I. Park, T. Hyeon, D. H. Kim, *Adv. Mater.* **2014**, *26*, 4825.
[5] Z. Song, W. Ye, Z. Chen, Z. Chen, M. Li, W. Tang, C. Wang, Z. Wan, S. Poddar, X. Wen, X. Pan, Y. Lin, Q. Zhou, Z. Fan, *ACS Nano* **2021**, *15*, 7659.
[6] P. Lei, Y. Bao, L. Gao, W. Zhang, X. Zhu, C. Liu, J. Ma, *Adv. Funct. Mater.* **2024**, *34*, 2313787.
[7] S. Sharma, G. B. Pradhan, A. Chhetry, K. Shrestha, T. Bhatta, S. Zhang, D. Kim, S. Jeong, Y. Shin, M. A. Zahed, X. Hui, J. Y. Park, *Nano Today* **2023**, *48*, 101698.
[8] S. Wang, J. Xu, W. Wang, G. N. Wang, R. Rastak, F. Molina-Lopez, J. W. Chung, S. Niu, V. R. Feig, J. Lopez, T. Lei, S. K. Kwon, Y. Kim, A. M. Foudeh, A. Ehrlich, A. Gasperini, Y. Yun, B. Murmann, J. B. Tok, Z. Bao, *Nature* **2018**, *555*, 83.
[9] P. Hu, F. Wu, B. Ma, J. Luo, P. Zhang, Z. Tian, J. Wang, Z. Sun, *Adv. Mater.* **2024**, *36*, 2310023.
[10] P. Hu, J. Wang, P. Zhang, F. Wu, Y. Cheng, J. Wang, Z. Sun, *Adv. Mater.* **2023**, *35*, 2207638.
[11] S. W. Dai, Y. L. Gu, L. Zhao, W. Zhang, C.-H. Gao, Y.-X. Wu, S.-C. Shen, C. Zhang, T.-T. Kong, Y.-T. Li, L.-X. Gong, G.-D. Zhang, L.-C. Tang, *Compos. B. Eng.* **2021**, *225*, 109243.
[12] Q. Chen, J. Zhao, J. Ren, L. Rong, P. F. Cao, R. C. Advincula, *Adv. Funct. Mater.* **2019**, *29*, 1900469.
[13] M. Gu, B. Zhao, J. Gao, X. Zhou, L. Huang, J. Wang, L. Wei, C. Yang, M. Chen, *Adv. Funct. Mater.* **2024**, *34*, 2400494.
[14] S. M. Xu, X. Y. Li, G. P. Sui, R. N. Du, Q. Zhang, Q. Fu, *Chem. Eng. J.* **2020**, *381*, 122666.
[15] C. Fragkogiannis, A. Koutsioukis, V. Georgakilas, *Molecules* **2022**, *27*, 3530.
[16] F. Qiang, L.-L. Hu, L.-X. Gong, L. Zhao, S.-N. Li, L.-C. Tang, *Chem. Eng. J.* **2018**, *334*, 2154.
[17] F. Qiang, S.-W. Dai, L. Zhao, L.-X. Gong, G.-D. Zhang, J.-X. Jiang, L.-C. Tang, *Sens. Actuators, B* **2019**, *285*, 254.
[18] W. Li, C. Li, G. Zhang, L. Li, K. Huang, X. Gong, C. Zhang, A. Zheng, Y. Tang, Z. Wang, Q. Tong, W. Dong, S. Jiang, S. Zhang, Q. Wang, *Adv. Mater.* **2021**, *33*, 2104107.
[19] C. F. Cao, B. Yu, J. Huang, X. L. Feng, L. Y. Lv, F. N. Sun, L. C. Tang, J. B. Feng, P. A. Song, H. Wang, *ACS Nano* **2022**, *16*, 20865.
[20] Y. Li, C.-F. Cao, S.-N. Li, N.-J. Huang, M. Mao, J.-W. Zhang, P.-H. Wang, K.-Y. Guo, L.-X. Gong, G.-D. Zhang, L. Zhao, L.-Z. Guan, Y.-J. Wan, L.-C. Tang, Y.-W. Mai, *J. Mater. Chem. A* **2019**, *7*, 27032.
[21] C. F. Cao, B. Yu, Z. Y. Chen, Y. X. Qu, Y. T. Li, Y. Q. Shi, Z. W. Ma, F. N. Sun, Q. H. Pan, L. C. Tang, P. Song, H. Wang, *Nano-Micro Lett.* **2022**, *14*, 92.
[22] H. Y. Chen, Z. Y. Chen, M. Mao, Y. Y. Wu, F. Yang, L. X. Gong, L. Zhao, C. F. Cao, P. Song, J. F. Gao, G. D. Zhang, Y. Q. Shi, K. Cao, L. C. Tang, *Adv. Funct. Mater.* **2023**, *33*, 2304927.
[23] C.-F. Cao, P.-H. Wang, J.-W. Zhang, K.-Y. Guo, Y. Li, Q.-Q. Xia, G.-D. Zhang, L. Zhao, H. Chen, L. Wang, J.-F. Gao, P. Song, L.-C. Tang, *Chem. Eng. J.* **2020**, *393*, 124724.
[24] Y.-Y. Wu, Z.-H. Wu, Z.-Y. Chen, L.-D. Peng, Z.-Q. Guan, Y. Li, C.-F. Cao, G.-D. Zhang, J.-F. Gao, P. Song, Y.-Q. Shi, L.-C. Tang, *Chem. Eng. J.* **2024**, *492*, 152183.
[25] G. Caminoa, S. M. Lomakinb, M. Lazzaria, *Polymer* **2001**, *42*, 2395.
[26] B. F. Guo, Y. J. Wang, Z. H. Qu, F. Yang, Y. Q. Qin, Y. Li, G. D. Zhang, J. F. Gao, Y. Shi, P. Song, L. C. Tang, *Small* **2023**, *20*, 2309272.
[27] Y. He, D. Wu, M. Zhou, Y. Zheng, T. Wang, C. Lu, L. Zhang, H. Liu, C. Liu, *ACS Appl. Mater. Interfaces* **2021**, *13*, 15572.
[28] W. Liu, Z. Chen, G. Zhou, Y. Sun, H. R. Lee, C. Liu, H. Yao, Z. Bao, Y. Cui, *Adv. Mater.* **2016**, *28*, 3578.
[29] E. Davoodi, H. Montazerian, R. Haghniaz, A. Rashidi, S. Ahadian, A. Sheikhi, J. Chen, A. Khademhosseini, A. S. Milani, M. Hoorfar, E. Toyserkani, *ACS Nano* **2020**, *14*, 1520.
[30] M. T. Chen, L. Zhang, S. S. Duan, S. Jing, H. Jiang, C. Li, *Adv. Funct. Mater.* **2014**, *24*, 7548.
[31] D. Sengupta, Y. Pei, A. G. P. Kottapalli, *ACS Appl. Mater. Interfaces* **2019**, *11*, 35201.
[32] S. Wu, J. Zhang, R. B. Ladani, A. R. Ravindran, A. P. Mouritz, A. J. Kinloch, C. H. Wang, *ACS Appl. Mater. Interfaces* **2017**, *9*, 14207.
[33] Q. Xia, S. Wang, W. Zhai, C. Shao, L. Xu, D. Yan, N. Yang, K. Dai, C. Liu, C. Shen, *Compos. Commun.* **2021**, *26*, 100809.
[34] F. Nie, Y. L. Gu, L. Zhao, L. T. Li, F. X. Shen, J. Song, J. Liu, G. D. Zhang, J. F. Gao, P. Song, Y. Shi, L. C. Tang, *Adv. Sensor Res.* **2024**, *3*, 2300140
[35] H. Li, J. Hu, R. Luo, K. Yang, B. Du, S. Zhou, X. Zhou, *ACS Appl. Mater. Interfaces* **2023**, *15*, 54933.
[36] X. Zhao, T. Li, H. Xie, H. Liu, L. Wang, Y. Qu, S. C. Li, S. Liu, A. H. Brozena, Z. Yu, J. Srebric, L. Hu, *Science* **2023**, *382*, 684.
[37] M. Mao, K.-X. Yu, C.-F. Cao, L.-X. Gong, G.-D. Zhang, L. Zhao, P. Song, J.-F. Gao, L.-C. Tang, *Chem. Eng. J.* **2022**, *427*, 131615.
[38] W. J. Hu, Q. Q. Xia, H. T. Pan, H. Y. Chen, Y. X. Qu, Z. Y. Chen, G. D. Zhang, L. Zhao, L. X. Gong, C. G. Xue, L. C. Tang, *Polymers* **2022**, *14*, 1628.
[39] H.-Y. Chen, Y. Li, P.-H. Wang, Z.-H. Qu, Y.-Q. Qin, L. Yang, J.-Y. Li, L.-X. Gong, L. Zhao, G.-D. Zhang, J.-F. Gao, L.-C. Tang, *Compos. Part A Appl. Sci. Manuf.* **2024**, *177*, 107907.
[40] Z. Guo, B. Long, S. Gao, J. Luo, L. Wang, X. Huang, D. Wang, H. Xue, J. Gao, *J. Hazard. Mater.* **2021**, *402*, 123838.
[41] L. Li, C. Jia, Y. Liu, B. Fang, W. Zhu, X. Li, L. A. Schaefer, Z. Li, F. Zhang, X. Feng, N. Hussain, X. Xi, D. Wang, Y. H. Lin, X. Wei, H. Wu, *Mater. Today* **2022**, *54*, 72.
[42] H. J. Zhan, K. J. Wu, Y. L. Hu, J.-W. Liu, H. Li, X. Guo, J. Xu, Y. Yang, Z.-L. Yu, H.-L. Gao, X.-S. Luo, J.-F. Chen, Y. Ni, S.-H. Yu, *Chem* **2019**, *5*, 1871.
[43] J. Guo, S. Fu, Y. Deng, X. Xu, S. Laima, D. Liu, P. Zhang, J. Zhou, H. Zhao, H. Yu, S. Dang, J. Zhang, Y. Zhao, H. Li, X. Duan, *Nature* **2022**, *606*, 909.
[44] G. Camino, S. M. Lomakin, M. Lageard, *Polymer* **2002**, *43*, 2011.
[45] J. Yang, S. Luo, X. Zhou, J. Li, J. Fu, W. Yang, D. Wei, *ACS Appl. Mater. Interfaces* **2019**, *11*, 14997.
[46] N. Bai, L. Wang, Q. Wang, J. Deng, Y. Wang, P. Lu, J. Huang, G. Li, Y. Zhang, J. Yang, K. Xie, X. Zhao, C. F. Guo, *Nat. Commun.* **2020**, *11*, 209.
[47] V. Liimatainen, D. M. Drotlef, D. Son, M. Sitti, *Adv. Mater.* **2020**, *32*, 2000497.
[48] J. Liu, Y. Sun, X. Zhou, X. Li, M. Kappl, W. Steffen, H. J. Butt, *Adv. Mater.* **2021**, *33*, 2100237.
[49] Y.-X. Qu, Q.-Q. Xia, L.-T. Li, C.-F. Cao, G.-D. Zhang, P. Castignolles, J. Bae, P. Song, J.-F. Gao, L.-C. Tang, *ACS Nano* **2024**, *18*, 22021.
[50] R. Verdejo, F. Barroso-Bujans, M. A. Rodriguez-Perez, A. Jose, M. Arroyo, M. A. J. J. o. M. C. Lopez-Manchado, **2008**, *18*, 3933.
[51] G.-D. Zhang, Z.-H. Wu, Q.-Q. Xia, Y.-X. Qu, H.-T. Pan, W.-J. Hu, L. Zhao, K. Cao, E.-Y. Chen, Z. Yuan, J.-F. Gao, Y.-W. Mai, L.-C. Tang, *ACS Appl. Mater. Interfaces* **2021**, *13*, 23161.

[52] X. C. Tian, S. Shaw, K. R. Lind, L. Cademartiri, *Adv. Mater.* **2016**, *28*, 3677.
[53] J. Yang, M. Li, S. Fang, Y. Wang, H. He, C. Wang, Z. Zhang, B. Yuan, L. Jiang, R. H. Baughman, Q. Cheng, *Science* **2024**, *383*, 771.
[54] W. Zhai, Q. Xia, K. Zhou, X. Yue, M. Ren, G. Zheng, K. Dai, C. Liu, C. Shen, *Chem. Eng. J.* **2019**, *372*, 373.
[55] Y. Shao, C. Luo, B. W. Deng, B. Yin, M.-b. Yang, *Nano Energy* **2020**, *67*, 104290.
[56] J. Yang, X. Liao, J. Li, G. He, Y. Zhang, W. Tang, G. Wang, G. Li, *Compos. Sci. Technol.* **2019**, *181*, 107670.
[57] Y. L. Zhang, C. G. Zang, Q. J. Jiao, *J. Appl. Polym. Sci.* **2020**, *137*, 49191.

